A Systemic Analysis of Multiscale Deep Convective Variability over the Tropical Pacific

WEN-WEN TUNG AND MITCHELL W. MONCRIEFF

National Center for Atmospheric Research, Boulder, Colorado*

JIAN-BO GAO

Department of Electrical and Computer Engineering, University of Florida, Gainesville, Florida

(Manuscript received 13 March 2003, in final form 26 January 2004)

ABSTRACT

The multiscale tropical deep convective variability over the Pacific Ocean is examined with the 4-month high-resolution deep convection index ($I_{T_{BB}}$) derived from satellite imagery. With a systemic view, the complex phenomenon is described with succinct parameters known as *generalized dimensions* associated with the correlation structures embedded in the observed time series, with higher-order dimensions emphasizing extreme convective events. It is suggested that convective activities of lifetimes ranging from 1 h to ~21 days have interdependence across scales that can be described by a series of power laws; hence, a spectrum of generalized dimensions, that is, the $I_{T_{BB}}$ time series is *multifractal.* The spatiotemporal features of the $I_{T_{BB}}$ time series is preliminarily examined by changing the spatial domain from $0.1^\circ \times 0.1^\circ$ to $25^\circ \times 25^\circ$. The multifractal features are weakened with increasing strength of spatial averaging but cannot be eliminated. Furthermore, the $I_{T_{BB}}$ data has the property of *long-range dependency,* implying that its autocorrelation function decays with a power law in contrast to the zero or exponentially decaying autocorrelation functions for white and commonly used red noise processes generated from autoregressive models. Physically, this means that intensified convection tends to be followed by another intensified event, and vice versa for weakened events or droughts. Such tendency is stronger with larger domain averaging, probably due to more complete inclusion of larger-scale variability that has more definite trends, such as the supercloud clusters associated with the Madden–Julian oscillation (MJO). The evolution of cloud clusters within an MJO event is studied by following the MJO system across the analysis domain for ~21 days. Convective activities along the front, center, and rear parts of the MJO event continuously intensify while approaching the date line, indicating multifractal features in the range of 1 h to about 5–10 days. Convective activity along the front and rear edges of the MJO event are more intermittent than in the center. The multifractal features of the $I_{T_{BB}}$ time series can be approximated by the random multiplicative cascade processes, suggesting likely mechanisms for the multiscale behavior and casting concern on the predictability time scale of the observed phenomena.

1. Introduction

Precipitating cumulus convection that extends throughout the troposphere prevails in most regions in the Tropics. It has been known to exhibit various spatial and temporal scales tied to tropical waves and disturbances (e.g., Chang 1970). Information about cloud-top temperature deduced from satellite imagery, such as outgoing longwave radiation (OLR), has been used as an index of deep convective activity in the Tropics. Takayabu (1994) and Wheeler and Kiladis (1999) performed wavenumber–frequency spectral analyses on the satellite imagery and found wave signals corresponding to the equatorially trapped waves (e.g., Matsuno 1966) in their theoretical dispersion relations. These results indicate that tropical deep convection is, to a certain degree, coupled with tropical wave motion. Wheeler and Kiladis (1999) also pointed out exceptional phenomena such as the tropical depression–type disturbances (TD; Takayabu and Nitta 1993) and the 40–60-day Madden–Julian oscillation (MJO; Madden and Julian 1971), which do not have theoretical counterparts in the wavenumber–frequency domain. The authors of both papers noted strong spectral broadening in their analyses. Salby and Hendon (1994) found similar broadening in the OLR power spectra in the frequency domain over the Indian Ocean–western Pacific sector (i.e., the warm pool), and commented that the background variance cannot be accounted for by simple white noise or first-order red noise processes.

The broadening of power spectra in addition to the

* The National Center for Atmospheric Research is sponsored by the National Science Foundation.

Corresponding author address: Dr. Wen-wen Tung, ASP/MMM, NCAR, P.O. Box 3000, Boulder, CO 80307-3000.
E-mail: wwtung@ucar.edu

MJO and TD suggest a very high degree of complexity in the convectively coupled tropical motions. One manifestation of the complexity is the multiscale (''hierarchical'') structure of tropical convection (Nakazawa 1988). Convective organization over the warm pool appears to have spatial sizes from $O(10^2)$ to $O(10^3)$ km and temporal scales from $O(1)$ to $O(10)$ days. In other words, the observed organizations range from mesoscale convective systems (MCSs) following the course of the diurnal cycle to organized supercloud clusters embedded in the eastward-propagating planetary-scale MJO. It is known that different scales of organizations tend to interlock (e.g., Nakazawa 1988; Lau et al. 1991; Weng and Lau 1994; Tung and Yanai 2002b). Mapes (1993) attributes such behavior to the existing MCSs laying out a favorable environment for subsequent MCSs through gravity wave dynamics. In a statistical description, the variance of the convection-coupled dynamic system spans a wide range of scales. Furthermore, it is spread in the self-similar manner as observed by satellite imagery across this temporal or spatial range, as suggested by Yano and Takeuchi (1987) and Yano and Nishi (1989).

Fractal and multifractal concepts provide a systemic description of complex dynamic phenomena. For instance, they have been developed to understand turbulence phenomena (Frisch 1995). Convection is one type of turbulent motion in the atmosphere. It differs from classic turbulence because of the effects of latent heating, whereas the latter is dominated by dissipative processes. Many quantities related to convective processes have fractal or multifractal characteristics, for example, the cloud liquid water content (Davis et al. 1996; multifractal), convective available potential energy (CAPE; Yano et al. 2001; fractal), and convective momentum transport (Tung and Yanai 2002a; fractal). Yano et al. (1996) examined the dependence of the fractal feature of convective organization on various cumulus parameterization methods. Using an OLR dataset with high spatial resolution, Pierrehumbert (1996) concluded that the *spatial* variability of the high cloud field over the tropical Pacific is multifractal. In particular, fractals and multifractals have been widely applied to the analysis and modeling of rainfall fields (e.g., Marsan et al. 1996; Over and Gupta 1996; Perica and Foufoula-Georgiou 1996; Veneziano et al. 1996; Schmitt et al. 1998), focusing on the rainfall in the mature stage of storm systems.

The goals of this work are to examine and describe the multiscale temporal variability of deep convective systems in the Tropics using the multifractal approach. The nature of this study is different from that concerning the multifractal aspects of conventional turbulence or the study of single storm systems. It involves the collective behavior and interaction of many multiscale convective systems coupled by dynamics field in the tropical environment. The deep convection index ($I_{T_{BB}}$) data used in this work is introduced in section 2. In section 3, the concepts and the working definition of multifractals as well as a set of construction rules of the random multiplicative cascade processes are discussed. In section 4, the $I_{T_{BB}}$ time series is analyzed and shown to have multifractal features that are captured by the multiplicative cascade processes. Various implications of this finding are discussed, including a reevaluation of the concept of signal-to-noise ratio and the consequences of applying different degrees of spatial and temporal averaging to the multifractal $I_{T_{BB}}$ time series. Random multiplicative cascade multifractals are known to have the property of long-range dependence. Therefore, in section 5, we study whether the $I_{T_{BB}}$ time series has similar properties. In section 6, temporal variability of deep convection inside the supercloud clusters that compose an MJO event is studied using the same multifractal analysis technique. Discussion and conclusions are presented in section 7.

2. The deep convection index

The equivalent blackbody temperature (T_{BB}) computed from the satellite-measured infrared (IR) irradiance through the earth's ''atmospheric window'' (wavelength = 10.5–12.5 μm) has been used to estimate cloud-top temperature. The estimation is particularly robust in the Tropics, where the coldest objects viewed from the space are most likely to be cloud tops. The T_{BB} intensity can infer the heights of these cloud tops and, further, separate very deep cloud types from shallower ones (Murakami 1983). The dataset used in this paper is the high-resolution, 0.1° × 0.1°, hourly deep convection index, $I_{T_{BB}}$, obtained during the Tropical Ocean and Global Atmosphere Coupled Ocean–Atmosphere Response Experiment (TOGA COARE; Webster and Lukas 1992) intensive observing period (IOP; November 1992–February 1993). The $I_{T_{BB}}$ index is derived from the Geostationary Meteorological Satellite (GMS) IR irradiance data, following the method in Nakazawa (1995):

$$I_{T_{BB}} = \begin{cases} (225 - T_{BB})/5, & \text{if } T_{BB} \le 225 \text{ K}, \\ 0, & \text{if } T_{BB} \ge 225 \text{ K}. \end{cases} \quad (1)$$

The horizontal coverage of the dataset is 15°S–15°N, 130°E–180°. Large values of $I_{T_{BB}}$ are positively correlated with high rainfall rates in the Tropics (e.g., Tung and Yanai 2002a). Therefore, if $I_{T_{BB}}$ time series is found to be multifractal, it is likely that rainfall has a similar behavior.

During the TOGA COARE IOP, the center of the deep convective activity is located slightly south of the equator. Figure 1 shows the time series of the hourly $I_{T_{BB}}$ averaged over the 5° × 5° region of 5°S–0°, 152.5°–157.5°E, which covers the TOGA COARE Intensive Flux Array (IFA; Fig. 2). Some of the data (less than 5%) in the time series are missing in early January and

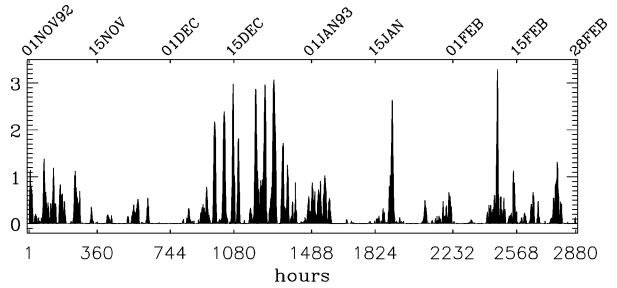

FIG. 1. The 5° × 5° averaged times series of $I_{T_{BB}}$ in the IFA region.

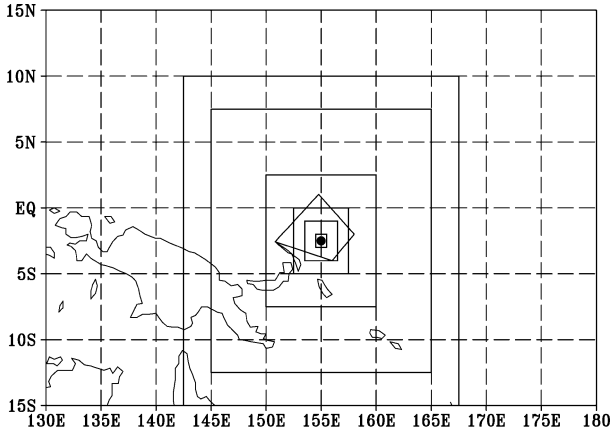

FIG. 2. Domain of analysis, with seven domains from a single point at 2.45°S, 154.95°E: 1° × 1°, 3° × 3°, 5° × 5°, 10° × 10°, 20° × 20°, to 25° × 25°. The polygon is the IFA.

are set to zero; this approach is reasonable considering that the missing period coincides with the low rainfall rate recorded by buoy data as well as with gauge- and satellite-based rainfall rates (Tung and Yanai 2002a).

In order to study the impact of spatial smoothing on the multifractal feature of the index, seven time series of $I_{T_{BB}}$ are prepared with different degrees of spatial smoothing: 0.1° × 0.1° (single point), 1° × 1°, 3° × 3°, 5° × 5°, 10° × 10°, 20° × 20°, and 25° × 25°. The averaging domains are centered at 2.45°S, 154.95°E, as plotted in Fig. 2. In section 7, a Lagrangian view is provided by tracking the $I_{T_{BB}}$ moving eastward with an MJO event in late December 1992, from 130°E to 180°. In the analysis, the $I_{T_{BB}}$ is averaged between 15°S and 10°N in order to capture the large latitudinal span of the propagating convective activity associated with MJO.

3. The multiplicative cascade process and the concept of multifractals

a. The multiplicative cascade model

The concepts of fractals and multifractals were first introduced by Mandelbrot (e.g., Mandelbrot 1974), and further developed to deepen the understanding of the intermittent turbulent phenomena (see Frisch 1995). The mathematical foundation of multifractal theories was provided by Hentschel and Procaccia (1983), Frisch and Parisi (1985), and Halsey et al. (1986), etc. Readers are referred to Gouyet (1996) for an excellent introduction.

Intuitively, a fractal set is a geometrical object with irregularities on all temporal and/or spatial scales. The geometrical object can be in physical space, such as a Cantor set (e.g., Mandelbrot 1982). It can also be used in phase space, such as chaotic attractors of dynamical systems. In atmospheric sciences, the usefulness of the concept of fractals concerns quantifying the scale dependence of physical variables and their spectral characteristics (e.g., Lilly 1983). Mathematically, a fractal is characterized by a power law, which is often called a scaling relation. A fundamental quantity that characterizes a fractal set is the fractal dimension. It is defined by the following simple and elegant scaling law:

$$N(\epsilon) \sim \epsilon^{-\alpha}, \ \epsilon \to 0, \tag{2}$$

where N represents the minimal number of boxes, of linear length not larger than ϵ, needed to cover the fractal set, and α is typically a noninteger number called the fractal dimension of the set. Fractal sets can be stochastic, that is, random fractals. One of the best known examples is Kolmogorov's $-5/3$ power law for the turbulent kinetic energy cascade in the inertial subrange (Kolmogorov 1941). Kolmogorov's law also belongs to the class of so-called $1/f$ stochastic processes, which are ubiquitous in both natural and man-made systems (e.g., Yano et al. 2001).

In essence, multifractals are characterized by many or infinitely many power-law relations. To migrate the notion of a fractal set to one that manifests multifractal measures, one may partition the fractal set into many (typically interwoven) subsets, each characterized by a power law. This can either be characterized by a spectrum of fractal dimensions (i.e., the generalized dimensions) with each dimension for one subset, as we will introduce shortly; or it can be characterized by singular measures, which, in concept, gives the relative "weight" of each subset. A fuller picture of multifractals can be established by constructing a multifractal field. Multifractals can be constructed by a multiplicative cascade process model. Since the $I_{T_{BB}}$ is a one-dimensional time series, the definition for a 1D random multiplicative cascade process model following the spirit of Biferale et al. (1994) is given here, which refers to the following generating rules.

1) At stage 0, consider a unit length. Associate it with a unit weight.
2) Divide the unit length into two (say, left and right) segments of equal length.
3) Also, divide the weight into two fractions, r and $1 - r$, and assign them to the left and right intervals, respectively. The parameter r, called the *multiplier*, is a random variable governed by a probability density function (pdf) $P(r)$, $0 \le r \le 1$.

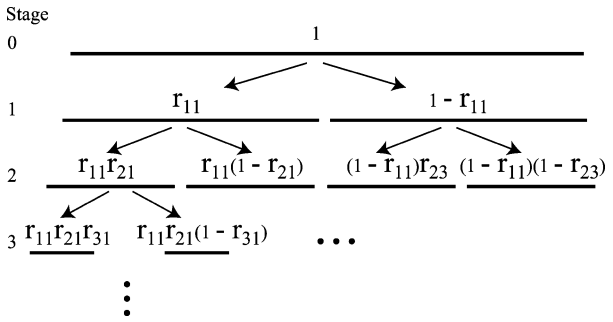

FIG. 3. Schematic diagram of the random multiplicative cascade process.

4) Each new interval and its associated weight are further divided into two parts following the same rules.

A scheme is shown in Fig. 3. At stage i, the length of the interval is 2^{-i}, and its associated multiplier is denoted as r_{ij} with $j = 1, \ldots, 2^i$. If the random multiplier distribution, $P(r)$, is assumed to be symmetric about $r = 0.5$ and have successive moments μ_1, μ_2, ..., then both r_{ij} and $1 - r_{ij}$ have marginal pdf $P(r)$. At stage N, the weights (i.e., the measures) are denoted as $\{w_n(N), n = 1, \ldots, 2^N\}$; each element is expressed as $w_n(N) = u_1 u_2 \cdots u_1 \cdots u_N$, where u_l, $l = 1, \ldots, N$, is either r_{ij} or $1 - r_{ij}$, $i = 1, \ldots, N$. Therefore, $\{u_l, l \geq 1\}$ are independent identically distributed (iid) random variables with pdf $P(r)$.

Note that the above scheme is sometimes called microcanonical multiplicative cascades, where the multipliers add up *exactly* to 1. One may require that the weights are preserved only *in terms of their expected value*. Such a scheme is sometimes called canonical multiplicative cascades, and can easily be constructed by generating two random variables, for example, r_{i1} and r_{i2}, where $E(r_{i1} + r_{i2}) = 1$, and a weight w_i at stage i is split into two parts, wr_{i1} and wr_{i2}. Multiplicative multifractals can even be nonconservative, as in Frisch (1995, p. 166). For our study, we shall employ the simplest conservative model, where weights simply add up to 1.

As an example, in Fig. 4 we have shown a portion (2880 points) of a realized field (4096 points) generated by a random multiplicative cascade process with stage number $N = 12$ and $P(r)$ given by

$$P(r) = \begin{cases} 2r + 0.5 & \text{if } 0 \leq r \leq 0.5 \\ -2r + 2.5 & \text{if } 0.5 \leq r < 1. \end{cases}$$

For random multiplicative cascade processes, at the stage N, a set of partition functions is computed as

$$\begin{aligned} M_q(\epsilon) &= \sum_{n=1}^{2^N} [w_n(N)]^q, \\ &= 2^N E\{[w_n(N)]^q\} = 2^N E[(u_1 u_2 \cdots u_N)^q] \\ &= 2^N \mu_q^N, \end{aligned} \tag{3}$$

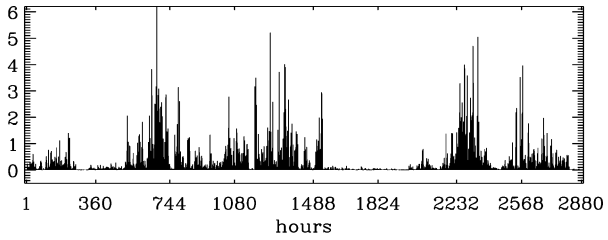

FIG. 4. The multifractal field generated by the random multiplicative cascade process.

with $E(\,)$ the expected value real q. Here μ_q is the qth moment of $P(r)$. A positive q value emphasizes large measures among w_n, while a negative q value emphasizes small measures. With large qs, M_q magnifies the intermittency and extreme events in the realization.

b. The definition of a multifractal field

The realization of the multiplicative cascade model has two properties that constitute our working definition of a multifractal field, which helps address the multiscale (hierarchical) structure of deep convective variability later in this paper. The first property is

$$M_q(\epsilon) \sim \epsilon^{\tau(q)}, \ \epsilon \to 0. \tag{4}$$

Equation (4) indicates scaling laws between various orders of partition function and the scale ϵ. In the case of the multiplicative cascade model, $\epsilon = 2^{-N}$ and $\tau(q) = -\ln(2\mu_q)/\ln 2$. If the measures w_n are uniform or only weakly nonuniform, the different emphases placed by q become trivial and the field is monofractal. In that case, $w_i = w \sim \epsilon$, and the number of terms in the summation in (3) is approximately ϵ^{-1}; therefore, $M_q(\epsilon) \sim \epsilon^{q-1}$ and $\tau(q) = q - 1$. Hence, the second property that determines a multifractal field is that the field has nonuniform measures, which can be estimated through the generalized dimensions:

$$D_q = \frac{\tau(q)}{q - 1}. \tag{5}$$

One may immediately notice that the computation of D_1 needs special attention because it is singular. Theoretically, one can employ l'Hôpital's rule, or use a Taylor series expansion for the numerator (e.g., Gouyet 1996). In practice, D_1 can sometimes be estimated via interpolation.

The first few dimensions of the dimension spectrum are of special interest. For instance, D_0 is the same as the fractal dimension α in (2), D_1 is called the information dimension, and D_2 is equivalent to the exponent of the power-law-decaying correlation function of the field (Hentschel and Procaccia 1983). When the measures are uniform or only weakly nonuniform (monofractal), D_q is independent of q and all D_q are reduced to the fractal dimension. This is equivalent to $\tau(q)$ being a linear function of q. When the measures are nonuni-

form (multifractal), D_q is a monotonically decaying function of q and $\tau(q)$ is a nonlinear function of q.

The above two properties or their similar forms are frequently used as the criteria to determine whether a dataset is multifractal (e.g., Davis et al. 1996; Ivanova and Ackerman 1999). However, the most strict definition of a multifractal field, as illustrated by the multiplicative cascade model, is that the multiplier distribution function $P(r)$ is stage independent. Given a sufficiently long dataset, it is possible to estimate $P(r)$ at different stages [e.g., Frederiksen et al. (1997), who used $O(10^5)$ samples]. This criterion is preferred since it is more free of artifacts. However, such datasets are rare in the atmospheric sciences.

If each measure, $w_n(N)$, in Fig. 4 is interpreted as the total convective activity in a time interval of length $2^{-N}T$, where T is the total time period of interest (2880 h), then the multiplicative cascade process becomes a primitive stochastic model for a time series of convective activity. Note the similarity between the intermittent features depicted in Figs. 1 and 4.

4. Multifractal characteristics of the $I_{T_{BB}}$ time series and implications

a. Multifractal characterizations

We now show that the multiscale $I_{T_{BB}}$ time series satisfies the two criteria that define it as a multifractal field. First, we compute the partition function, $M_q(\epsilon)$, and check if the following scaling relations hold

$$M_q(\epsilon) = \sum_i w_i^q = 2^N \langle w_i^q \rangle \sim \epsilon^{\tau(q)}, \quad \text{as } \epsilon \to 0 \qquad (6)$$

for real values of q, where $\epsilon = 2^{-N}$, $N = 1, 2, \ldots, 11$, and $\langle w_i^q \rangle$ is the ensemble average of w_i^q. In order to compute (6), the total number of data points should have a base number of 2. We use 2048 points for computation each time. The computation is done twice, for the first and the last 2048 points in the $I_{T_{BB}}$ time series, respectively. For each computation, the total length as well as measure (weight) of the 2048 points are normalized to 1. The normalization of the weight yields $\Sigma_i w_i = 1$, which implies that $\tau(1) = 0$ is the trivial scaling relation for M_1.

Figure 5a shows $-\log_2 M_q(\epsilon)$ versus $-\log_2 \epsilon$ for the $5° \times 5°$ averaged $I_{T_{BB}}$ time series (Fig. 1). Only M_q functions with $q \geq 0$ are shown since we are more interested in the large measures (intermittency) in the $I_{T_{BB}}$. Computations that utilize different portions of the time series produce similar results. With linear regression, we clearly observe a series of power laws for different values of q. The power-law exponents, $\tau(q)$, are the slopes of the regressed lines. The regression lines fit less well for large values of q (e.g., $q = 6$) due to much rarer samples of extreme events. When $\epsilon = 2^{-1}$, there are only two measures to evaluate (6) in each computation, so the resulting points are not used in the linear regressions. Nevertheless, in Fig. 5a, these points lie nicely on the regression lines for $q = 0$, 1, and 2. The scaling relations thus identified correspond to the time scales from 1 to at least 512 h (~21.3 days, see the top of the figure, where the correspondence between the scale ϵ and the physical time is shown). The breakdown of scaling relations beyond 512 h could be due to insufficient sampling.

The second step toward characterizing the $I_{T_{BB}}$ dataset as multifractal is to check the degree of nonuniformity of the measures (w_i). Figure 5b shows the variation of $\tau(q)$ against q, in which $\tau(q)$ is the mean value of the power-law exponents of $M_q(\epsilon)$ derived from both portions of the data. The error bars defined by the standard deviations of the estimated power-law exponents of both data portions are plotted, indicating that the power laws are reasonably satisfied even for large q. In contrast to the reference straight line in the figure, $\tau(q)$ forms a concave curve. Hence, it is no surprise that the D_q shown in Fig. 5c (in which D_1 is interpolated from $D_{0.5}$ and $D_{1.5}$) is a monotonically decaying nonlinear function of q. The second criterion necessary for the $I_{T_{BB}}$ time series to be multifractal is thus satisfied.

In Figs. 5b,c, the broken curves depict the $\tau(q)$ and D_q functions obtained from the model time series (Fig. 4). In the model, the $\tau(q)$ behaves similarly to that of the observed $I_{T_{BB}}$ time series, with the exception that at larger values of q, the model $\tau(q)$ arches toward the abscissa. This tendency is reflected in D_q. In Fig. 5c, the model D_q is a more steeply declining curve, whereas the observed D_q shows a tendency to remain constant with larger q. This therefore indicates that the observed $I_{T_{BB}}$ time series contains fewer extreme events than the model time series. It is also noted that the fractal dimension (D_0) is 1.0 for the model and ~0.97 for the observation. This is a fundamental difference between the model and the observed time series. By definition, the multiplicative cascade model can produce infinitesimally small positive measures but never zeros, which explains the fractal dimension of the model result. However, zeros are present when no significant deep convection is recorded in the $5° \times 5°$ observational domain. The smaller than 1.0 fractal dimension indicates the sparseness of the observed $I_{T_{BB}}$ time series.

The $I_{T_{BB}}$ time series contains information on multiscale tropical convection-coupled waves and disturbances. The multiplicative cascade model captures the multifractal characteristics of the $I_{T_{BB}}$ time series reasonably well. As demonstrated by the model, multifractals can be created through the scale-invariant multiplicative process. In the tropical atmosphere, the multiplicative process could be partly responsible by continuous stretching and folding of dynamic and thermodynamic fields through the change of momentum and vorticity fields across various scales induced by convective updrafts and downdrafts. For example, over the same observation domain and period, convection has been found to generate perturbations of vorticity

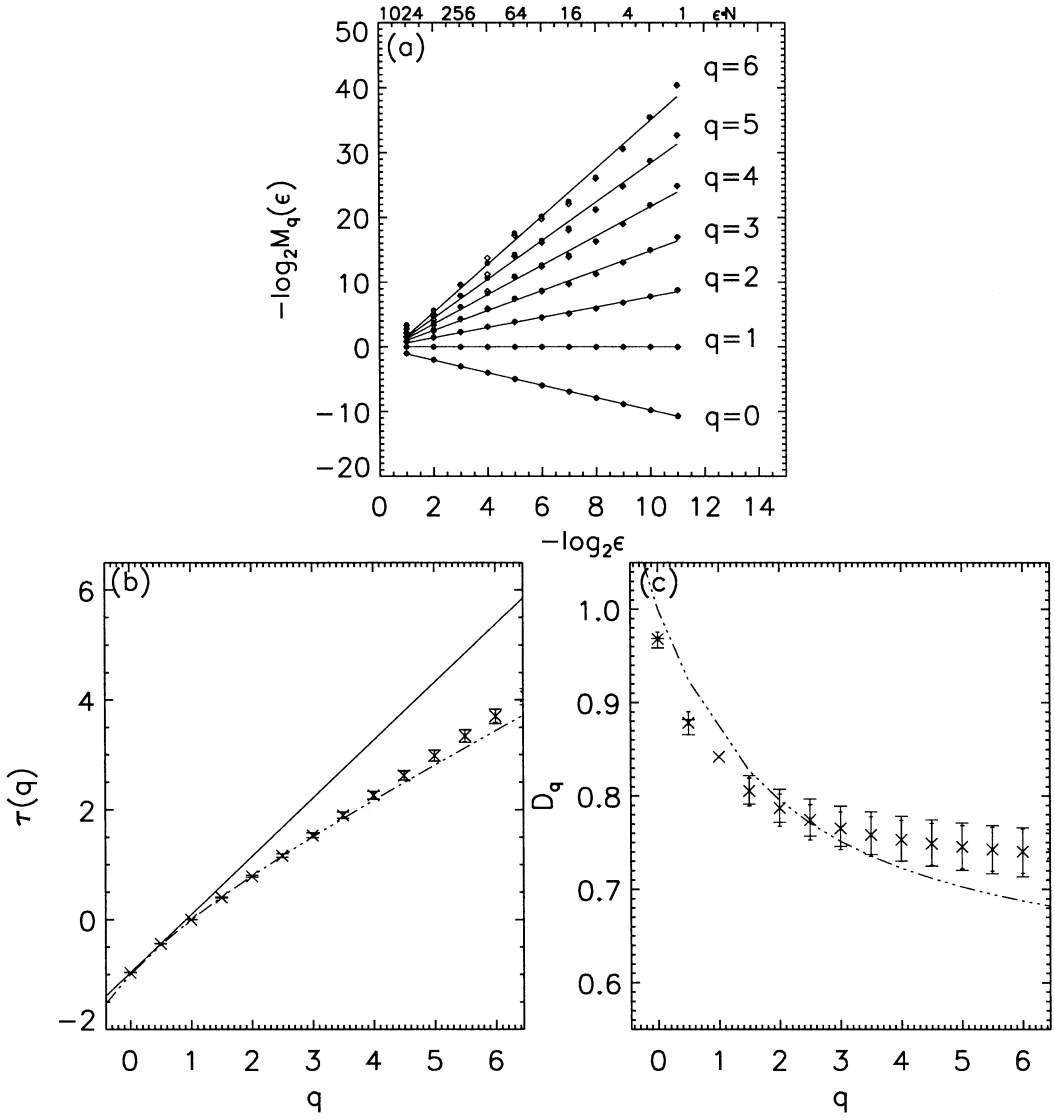

FIG. 5. Derived from the 5° × 5° $I_{T_{BB}}$ time series (a) the partition function $M_q(\epsilon)$; solid circles and open diamonds are results from the first and last 2048 points of the time series, respectively; straight lines are best-fit lines of solid circles. (b) The $\tau(q)$ obtained from both portions of the dataset, with wide error bars indicating plus and minus one std dev from the estimated exponent using the first 2048 points; thin error bars, the last 2048 points. The broken line is $\tau(q)$ from the random multiplicative cascade model. (c) Generalized dimensions D_q, with similar symbols as in (b); D_1 is interpolated without accompanying error estimates.

from the convection to large scales through modifying the momentum field (Tung and Yanai 2002a,b).

b. Consequence of spatial averaging

We now examine the impact of spatial averaging on the multifractal features of the $I_{T_{BB}}$ time series. In Fig. 6, seven domain-averaged $I_{T_{BB}}$ time series are plotted, with increasing domain size from top to bottom. The scale of the *y* axis is adjusted for domains 10° × 10° to better appreciate the variations of the time series. Although the spatial averaging appears to smooth the time series significantly, the irregularity within the time series is preserved. In fact, scaling relations held by the partition function of the 5° × 5° dataset are similarly found in other time series. This finding also confirms the conjecture by Yano et al. (2001) that the $1/f$ stochastic behavior of tropical convective variability should remain robust even after large-scale spatial averaging.

Figure 7 shows the generalized dimensions (D_q) of the seven domain-averaged time series, which are plotted as in Fig. 5c. The small error bars for D_q in the larger domains indicate that the scaling relations are more well defined there. Functions D_q of larger domain averages descend more slowly with q than those of

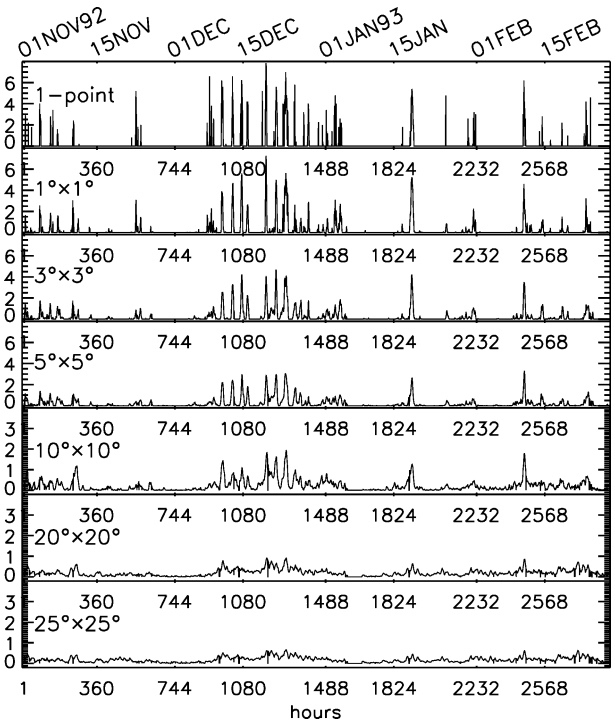

FIG. 6. (top to bottom) Averaged time series over 0.1° × 0.1°, 1° × 1°, 3° × 3°, 5° × 5°, 10° × 10°, 20° × 20°, and 25° × 25° domains. The vertical scale is enlarged for the last three domains.

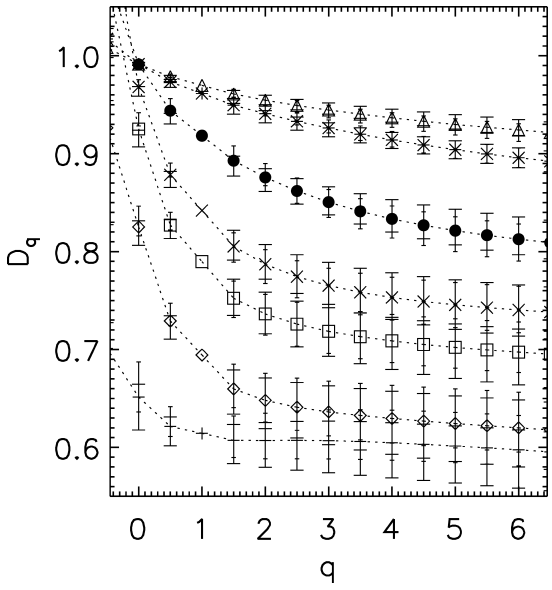

FIG. 7. Generalized dimensions D_q for the $I_{T_{BB}}$ time series: + = 0.1° × 0.1°, ◇ = 1° × 1°, □ = 3° × 3°, × = 5° × 5°, ● = 10° × 10°, * = 20° × 20°, and △ = 25° × 25°.

smaller domain averages, particularly at smaller q values. This suggests that spatial averaging reduces the significance of the multifractal characteristics of the time series but does not eliminate it completely. The D_q for the single-point dataset appears to be horizontal with $q \geq 2$, most likely the result of insufficient samples, particularly those of relatively extreme events, since the time series is most sparse. Such deficiency in sampling is also reflected by the large error bars for the D_q estimation. Furthermore, with the same q, larger-domain averages have bigger D_q. This may reflect that physical processes with better-defined long-range trends are dominant in the time series of larger-domain averaging. This aspect will be discussed along with the variance–time relations in section 5.

c. Consequence of temporal smoothing

A rather common picture of data analysts is: $x(t) = y(t) + n(t)$, where $y(t)$ is the true signal, $n(t)$ is the measurement noise, often taken as white, and $x(t)$ is the observed signal. One might expect $x(t)$ to have a well-defined mean when averaged over a long enough period of time, while its standard deviation is insignificant when compared with the mean; or, by applying a moving average, seemingly ''transient'' noise could be removed. This picture is at least partly true, since measurement noise is always present. However, the averaging or smoothing tactic may not be as constructive as expected, especially when the true signal displays multifractal features. This is because the variations of $y(t)$ over a broad range of time scales are the intrinsic features of such processes, as succinctly and precisely captured by the definition of multifractal in (6). More concretely, the variance and transient features of $x(t)$ are driven from both $y(t)$ and $n(t)$. While the contribution from $n(t)$ may be negligibly small when the average is taken over a long time interval, the contribution from $y(t)$ can nevertheless be quite large. Often, the mean of the signal can be much smaller than its standard deviation. In some cases, the mean of $x(t)$ may not even be well defined.

We can quantify how effective it is to temporally smooth the $I_{T_{BB}}$ time series by averaging the 5° × 5° time series over successively long time windows. For comparison, we also apply the same methods to the realization of the random multiplicative cascade model (Fig. 4), a white noise process (Fig. 8a), and a ''shuffled'' 5° × 5° $I_{T_{BB}}$ time series (Fig. 8b). White noise is defined as $y_i = 1.0 + n_i$. Time series n_i is obtained through a random number generator with mean and standard deviation equal to 0.0 and 0.25, respectively. The shuffling of the $I_{T_{BB}}$ time series is enabled by the following: (i) A sequence of uniformly distributed random variables, with length equal to that of the $I_{T_{BB}}$ time series, is generated. (ii) The random time series is sorted according to the magnitude of its elements. (iii) Suppose the ith element of the random sequence ranks the jth largest (or smallest), then the ith element of the $I_{T_{BB}}$ time series becomes the jth element of the shuffled time series.

Figures 9a–d show the results of daily and monthly nonoverlapping window averages for all four time series. Standard deviations are plotted along with the

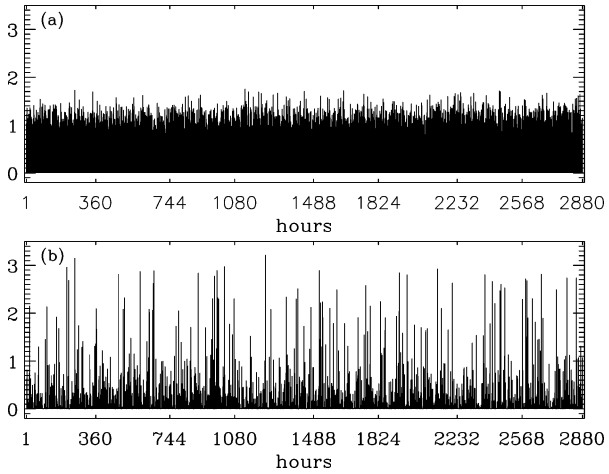

FIG. 8. Time series of (a) white noise process and (b) shuffled 5° × 5° $I_{T_{BB}}$ time series.

monthly averages. Evidently, the window averages become well-defined much sooner in the white noise process and shuffled $I_{T_{BB}}$ in Figs. 9c,d than the time series in Figs. 9a,b. In Figs. 9a,b, both monthly averages and standard deviations exhibit considerable variations from window to window. Figure 9a might be expected given that the slowest cycle resolved in the 120-day $I_{T_{BB}}$ time series is the 60-day signal of the MJO, so naturally the monthly mean values should vary. However, it is interesting but subtle that the $I_{T_{BB}}$ time series, as well as the random multiplicative cascade process, has a property called long-range dependence. This can be observed physically as a spectrum of smaller-scale convection-coupled waves and disturbances being enhanced at the convective phase of MJO, as implied by the large standard deviation in December in Fig. 9a.

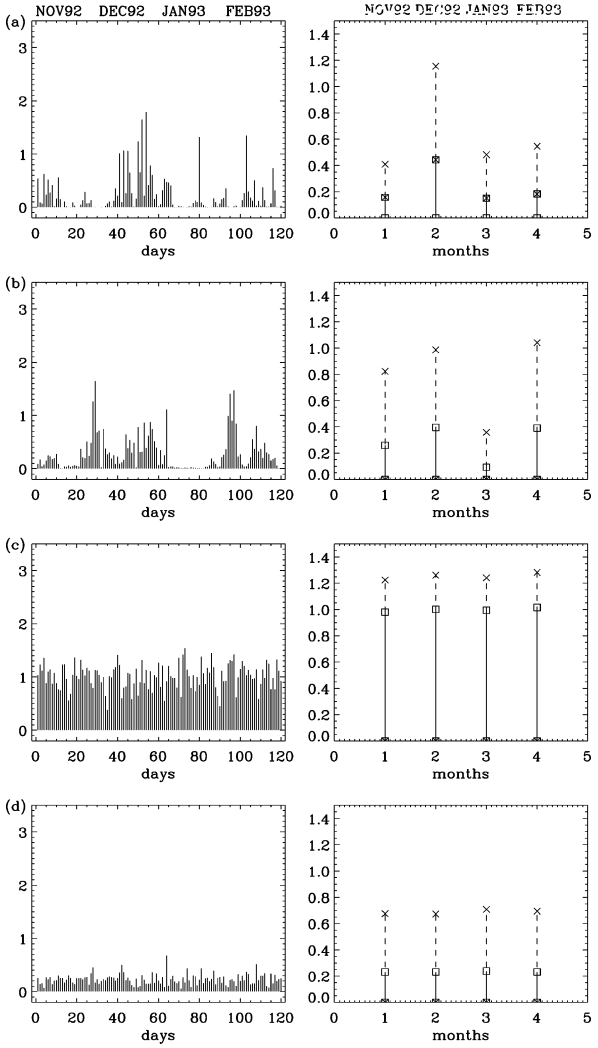

FIG. 9. Daily (24 samples) and monthly (720 samples) window averages (solid lines) of (a) $I_{T_{BB}}$, (b) random multiplicative cascade process, (c) white noise process, and (d) randomly shuffled 5° × 5° $I_{T_{BB}}$ time series, as well as standard deviations (dashed lines) plotted with monthly averages.

5. Long-range dependence

a. Long-range dependence in the variance–time relation

In this section, we introduce an interesting property called long-range dependence in the $I_{T_{BB}}$ dataset. A random multiplicative cascade multifractal has long-range dependence. Such dependence is conventionally characterized by the strength of a so-called Hurst exponent (e.g., Mandelbrot and Van Ness 1968; Mandelbrot 1982). Moving averages are far less effective in removing irregularities from such time series or spatial fields than from white noise processes. Gao and Rubin (2001) found that the Hurst exponent is closely related to the second moment of the pdf for the multiplier $[P(r)]$, as implied by the last line in Eq. (3).

The property of long-range dependence can be quantified independently from the partition function technique used in sections 3 and 4. Here, we start by further formalizing the phenomenon exhibited by Fig. 9. Given a time series, $X = \{X_i : i = 0, 1, 2, \ldots\}$, for each $m = 1, 2, 3, \ldots$, let $X^{(m)} = \{X_i^{(m)} : i = 1, 2, 3, \ldots\}$ denote the new time series obtained by averaging the original series X over nonoverlapping blocks of size m, that is,

$$X_i^{(m)} = (X_{im-m+1} + \cdots + X_{im})/m, \qquad i \geq 1. \quad (7)$$

For each time series $X^{(m)}$, we can compute its variance. For a white noise process, $\mathrm{var}[X^{(m)}] \sim m^{-1}$. For a random process with an exponentially decaying autocorrelation function, the relation $\mathrm{var}[X^{(m)}] \sim m^{-1}$ still holds when m is not too small: $\mathrm{var}[X^{(m)}] \sim m^{-1}$. This feature is readily verified with the presently quite short time series, as shown in the dashed line in Fig. 10. On the other hand, $\mathrm{var}[X^{(m)}]$ for all seven $I_{T_{BB}}$ time series decay with m much more slowly, as shown by the solid lines in Fig. 10. We find that for the $I_{T_{BB}}$, $\mathrm{var}[X^{(m)}] \sim m^{2H-2}$,

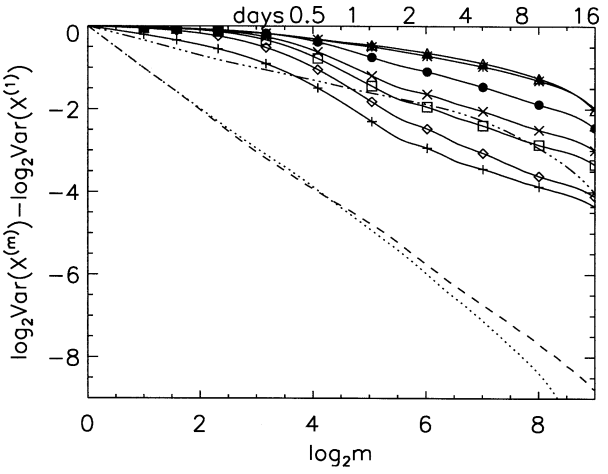

FIG. 10. Variance–time plot for seven $I_{T_{BB}}$ time series (solid, with the same symbols as in Fig. 7), random multiplicative cascade process (dot–dot–dashed), white noise process (dashed), and randomly shuffled $5^\circ \times 5^\circ$ $I_{T_{BB}}$ time series (dotted). Corresponding window sizes in days are shown at the top.

with $H = \sim 0.75$–0.9. Following the definition in Mandelbrot and Van Ness (1968), the parameter H is the Hurst exponent. Mathematically, the autocorrelation function for these processes decays with a power law: $r(k) \sim k^{2H-2}$, for large lag k [see derivation in Mallat (1999), section 6.4.3]. Note that when $H > 1/2$, the summation of $r(k)$ goes to infinity, $\Sigma_{i=1}^{\infty} r(k) \to \infty$. This quantifies the terms ''long memory'' or ''long-range dependence.''

To better appreciate that $\text{var}[X^{(m)}] \sim m^{-1}$ is alone true for short-range-dependent (in contrast to long-range dependent) red noise processes, we have simulated an autoregressive (AR) model defined by

$$A_{n+1} - \overline{A} = a(A_n - \overline{A}) + \eta_n, \qquad 0 < a < 1, \quad (8)$$

where $\overline{A}$ is the mean for the process A_n, constant a is an autoregressive coefficient, and η_n is a Gaussian random process with zero mean. One can readily show that the autocorrelation function for such a process decays exponentially, $r(k) = a^k = e^{k\ln a}$. Autoregressive models like this have been used to model red noise process, for example, in convective heating by Lin and Neelin (2002).

Figure 11a plots a time series with length 2880 generated from such a process with $a = 0.97$, which is the lag-1 autocorrelation coefficient of the $5^\circ \times 5^\circ$ $I_{T_{BB}}$ time series. Negative values in the time series can be truncated to further approximate the $I_{T_{BB}}$ time series. One may justify such truncation by picturing that the red noise represents vertical velocity, while only upward motion produces rainfall, which is related to the $I_{T_{BB}}$. The time series in Fig. 11a is significantly different from the white noise and much more like the actual $I_{T_{BB}}$ time series, although it is still an inferior model to the multiplicative process in term of its ability to capture intermittency.

Figure 11b shows variance–time plots of the red noise processes from the AR model with $a = 0$ (white noise), 0.1, 0.5, 0.7, 0.9, 0.97, and 0.97 with only positive values, in addition to that of the $5^\circ \times 5^\circ$ $I_{T_{BB}}$ time series. The truncation of negative values for the $a = 0.97$ process results in little difference in this figure. We observe from the figure that when a is much smaller than 1, the H value is very close to 1/2 for the entire range of m. When a is close to 1, however, H assumes a value of 1 when m is small. Thus, $H = 1$ implies a perfect correlation. This can be understood by noticing that when a is very close to 1, the value of A_n is somewhat directly passed to the value of A_{n+1}, resulting in a nice memory. Now it is clear that the region of m with $H = 1$ increases with the increasing of the coefficient a. However, even when a is as large as 0.97, the process still soon assumes an H value of 1/2 when m is not too small. These observations can be rigorously proven, for example, in Kaulakys and Meskauskas (1998). It is interesting to note that such AR processes with the coefficient a very close to 1 as well as other more general autoregressive and moving-average (ARMA) models (Box and Jenkins 1976) are sometimes used to model a random process with certain memory (Kaulakys and Meskauskas 1998). However, such processes are not very effective in describing processes with very long memory, since their autocorrelation functions decay exponentially.

The AR model is not entirely without merits. As indicated in Figs. 10 and 11b, the rate of decreasing variance versus increasing time interval m of the $5^\circ \times 5^\circ$ $I_{T_{BB}}$ within around 1 day is better captured by the AR model with $a = 0.9$ than the multiplicative cascade process. It is possible that for modeling the second-order statistics of convective activities at time scales within $\sim$1 day, an AR model like the one shown in this paper (i.e., $a = 0.9$) may be sufficient. We note however, that $a = 0.9$ is smaller than the actual lag-1 correlation of the $I_{T_{BB}}$ time series, which is 0.97. Also note that its ability to produce any longer-range dependence as well as intermittency is mathematically limited. The multiplicative cascade process, however, has a much greater potential to be tuned into a desired fit to the real data in terms of not only the variance–time property but also the multifractal dimensions.

b. Properties associated with long-range dependence

Mandelbrot and Van Ness (1968) coined the term ''fractional Brownian motions'' (fBms) for an extended family of statistically self-similar Gaussian functions characterized by the Hurst exponent, H, $0 < H < 1$. For ordinary Brownian motion (Bm, a nonstationary process), $H = 1/2$. White Gaussian noise is the derivative of the Bm; similarly, the fractional Gaussian noise (fGn) is the derivative of the fBms. The fBm family is often called the random-walk-type process, while the fGn is called the increment process. Both provide useful models for natural phenomena containing both macro-

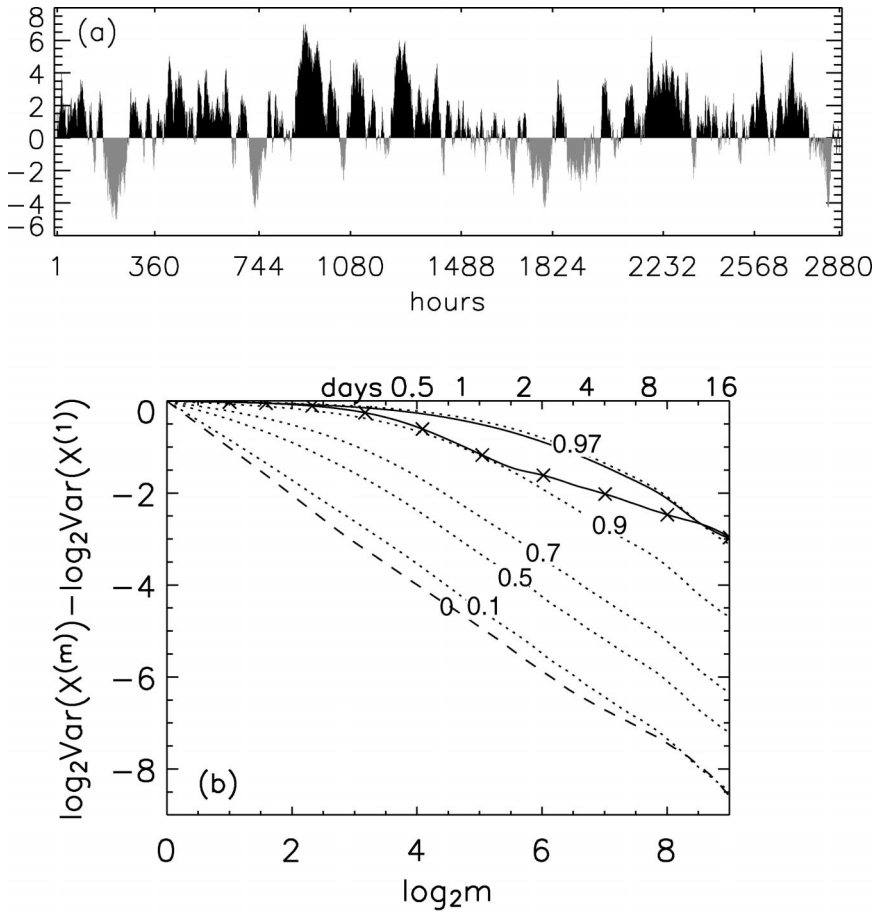

FIG. 11. (a) Time series of the AR model with $a = 0.97$ and (b), similar to Fig. 10, the variance–time relation of the model (dotted line) with $a = 0.1$, 0.5, 0.7, 0.9, 0.97, and 0.97 with only positive values (solid overlapping line), in addition to those of the $5^\circ \times 5^\circ$ $I_{T_{BB}}$ time series (solid line with "×") and the white noise process (dashed, $a = 0$).

and microscales. The fGn is a much simplified prototype to address the power-law decaying autocorrelation function and power spectrum of the $I_{T_{BB}}$ as well as X time series in this study.

Furthermore, when the variance–time relation $\mathrm{Var}[X^{(m)}] \sim m^{2H-2}$ holds, through the Weiner–Khinchin theorem (Monin and Yaglom 1975), the power spectral density (PSD) for the time series X decays in a power-law manner: $\mathrm{PSD}_X(f) \sim 1/(f^{2H-1})$, with f the frequency. The PSD for the time series $Y = \{Y_n : n = 0, 1, 2, \ldots\}$, with $Y_n = \Sigma_{i=1}^{n} X_i$ an integration of X, can be proven to decay as $\mathrm{PSD}_Y(f) \sim 1/(f^{2H+1})$. These power-law-decaying PSDs justify the term of $1/f$ stochastic processes (e.g., Yano et al. 2001). It is noted that when $H = 1/2$, then the PSD for X (the white Gaussian noise) is flat, while that for Y (the Bm) is $1/f^2$. The X time series is also often denoted as an increment process, while the Y time series as a random-walk-type process.

Suppose the mean value of the increment process $X = \{X_i : i = 0, 1, 2, \ldots\}$ is $\mu(x)$. If $0 \le H < 1/2$, then when $X_j > \mu(x)$, it will be more likely to have $X_{j+1} < \mu(x)$. If one takes $X_j - \mu(x)$ as the jump at time j, a jump-up is more likely followed by a jump-down when $0 \le H < 1/2$. This is called the *antipersistent correlation.* The integration of X leads to a random-walk-type process (fBm) that is less nonstationary than the Bm. Conversely, if $1/2 < H < 1$, then the times series X has the *persistent correlation,* or long-range dependence: a jump-up is more likely followed by another jump-up at the next time step, so is a jump-down followed by another jump-down. The integration X generates a random-walk-type process that is more nonstationary than the Bm.

Since $1/2 < H \le 1$ for all seven $I_{T_{BB}}$ time series, we conclude that the $I_{T_{BB}}$ datasets possess the long-range dependence properties. As previously mentioned, during the IOP, smaller-scale convection-coupled waves and disturbances are enhanced during the convectively active phase of MJO. In observations, convective incidents associated with these waves/disturbances also gain intensity during this phase of the MJO until the full bloom of a westerly wind burst (WWB) that marks the end of this phase (e.g., Yanai et al. 2000). Interestingly, the

long-range dependence in the 5° × 5° $I_{T_{BB}}$ data is well captured by the random multiplicative cascade model, as shown by the dash–dot–dot line in Fig. 10. Now it should be clear why temporal smoothing of the $I_{T_{BB}}$ time series cannot yield really smooth results. Moreover, the long-range dependence is more significant with a larger-domain average, according to the slopes of solid lines in Fig. 10, while the values of D_2 in Fig. 7 provide the same information. This may be due to the fact that larger domains encompass larger-scale variability that displays longer-range dependence.

In Fig. 10, the shuffled 5° × 5° $I_{T_{BB}}$ time series yields a similar slope to the white noise process. Evidently, the shuffling has destroyed the long-range dependence in the original time series. It is noted that the shuffling destroys all kinds of correlation in the original time series but preserves the original pdf, thus information of pdf is not sufficient to realize a fractal or multifractal process.

The pdf of $I_{T_{BB}}$ time series is expected to be non-Gaussian with a thick-tailed distribution, as indicated by the importance of higher-order partition functions. That means, extreme events of convective activity contribute significantly to the variability of the time series. However, given the currently short time series, it is difficult to quantify the pdf of $I_{T_{BB}}$ by computation, since those extreme events are considered too rare. It is important, however, to note that the non-Gaussian nature of $I_{T_{BB}}$ does not necessarily contribute to the multifractal variation we observe. A supporting example is that the pdf of Levy flight (Mandelbrot 1982) has a power-law tail, which is non-Gaussian; the process is nevertheless monofractal. As seen in Fig. 10, the shuffled 5° × 5° $I_{T_{BB}}$ time series yields a similar slope to the white Gaussian noise. Apparently, the shuffling has destroyed the long-range dependence in the original time series. In fact, the shuffling destroys all kinds of correlation in the original time series but preserves the original pdf, thus information of pdf is not sufficient to realize a fractal or multifractal process.

6. Variation of deep convective intensity in the MJO

Thus far the time series examined represent the local (Eulerian) time change of deep convective activity. An intriguing question is how deep convection evolves inside a large-scale coherent dynamic system such as the MJO. Therefore, in this section, multifractal analysis is applied Lagrangian-wise to time series of $I_{T_{BB}}$ within the eastward-moving envelope of the first MJO event observed during TOGA COARE IOP. In order to properly account for the large latitudinal span of the MJO structure, the $I_{T_{BB}}$ is averaged between 15°S and 10°N. The time–longitude section of averaged $I_{T_{BB}} \geq 0.5$ is shown in Fig. 12. The 0.5 threshold, which preserves approximately the top 20% of the deep convective events, is selected to outline the center of the propagating MJO.

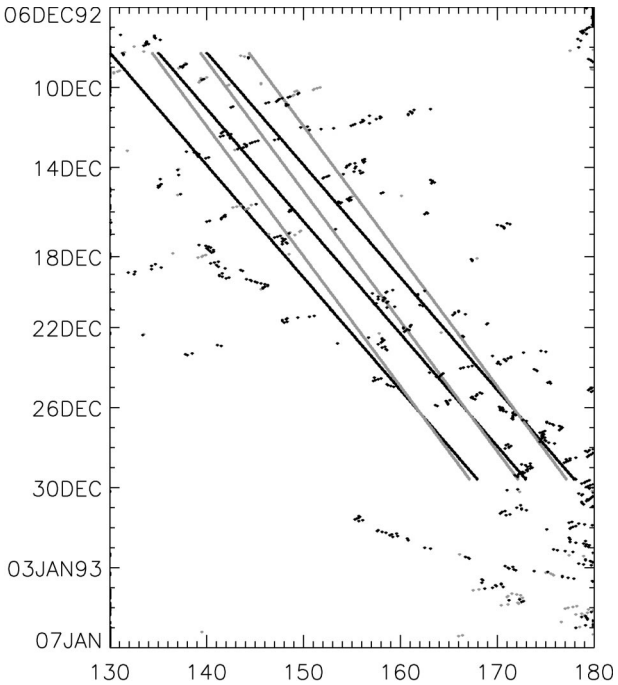

FIG. 12. Time–longitude section of $I_{T_{BB}}$ averaged between 15°S and 10°N. The data points shown are $I_{T_{BB}} \geq 0.5$, among which the black points are $I_{T_{BB}} \geq 0.8$. The center gray and black best-fit lines, respectively, determine the center axis of the MJO envelope defined by the 0.5 and 0.8 thresholds from 0700 UTC 8 Dec to 1400 UTC 29 Dec. The other lines define the parts of the envelope that are 5° in front and behind the center axis.

Moreover, the darker points in the figure are $I_{T_{BB}} \geq 0.8$, which represent the top 10% of the events. The center of the eastward-moving envelope and the propagation speed of the MJO is determined by linear regression of the points. In Yanai et al. (2000), the overall group velocity of the MJO event from the eastern Indian Ocean to the date line is about 5 m s^{-1}, although local variation occurs. Movement of convection significantly slows down upon approaching the date line, and eventually ceases around the date line. In Fig. 12, the group velocity of convective activity is approximately 1.9 (based on the 0.5 threshold) to 2.3 m s^{-1} (0.8 threshold) during the 512-h period from 0700 UTC 8 December to 1400 UTC 29 December, as indicated respectively by the gray and black best-fit lines in the center of Fig. 12. After the center axis of the MJO is determined, the front and rear parts of the entire envelope are represented by the data points leading and lagging 5° away from the center, respectively.

Figure 13 shows the time series of deep convective activity moving along the front (dashed line), center (solid line), and rear (dotted line) parts of the MJO obtained from (a) the 0.5 and (b) the 0.8 thresholds. Evidently, the threshold selections do not yield qualitatively different results. Both Figs. 13a,b show a ''shift of regime'' in terms of convective intensity around 18 December, as the major part of the MJO event moves

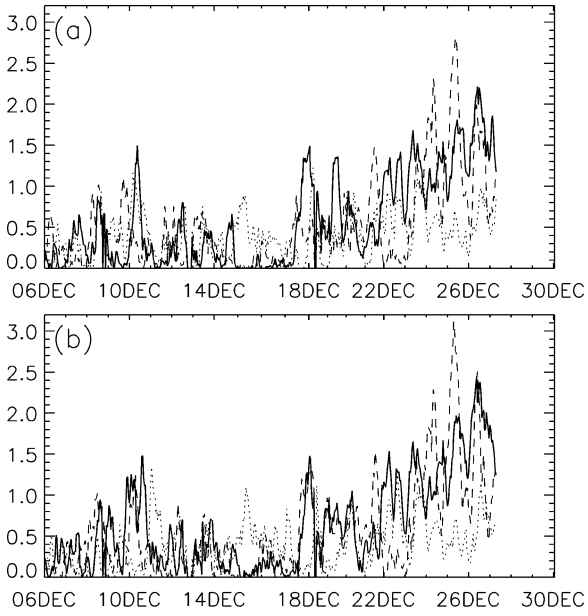

FIG. 13. The $I_{T_{BB}}$ time series on the center axis of the MJO envelope in Fig. 12 (solid line) determined by the (a) 0.5 and (b) 0.8 thresholds, are and those leading (dashed line) and lagging (dotted line) the axis by 5°.

past 150°E. After 18 December, the convection time series becomes more nonstationary with increasing intensity, possibly associated to the property of long-range dependence observed in section 5. The regime shift is more obvious in the front and center parts of the MJO envelope than in the rear.

Using (6), the partition functions $[M_q(\epsilon)]$ for these time series are calculated with $\epsilon = 2^{-N}$, $N = 1, 2, \ldots, 9$. Figure 14a shows the log–log plots of $M_q(\epsilon)$ derived from the $I_{T_{BB}}$ time series in the front (diamond), center (solid circle), and rear (cross) parts of the MJO event determined by the 0.5 threshold. These partition functions all follow power laws in the range of 1 h to around 5–10 days. Known physical phenomena within this temporal range include diurnal cycles, quasi-2-day waves, gravity waves, mixed Rossby–gravity waves, Rossby waves, and TD-type disturbances. The generalized dimensions [D_q, see Eq. (5)] of these time series are computed and shown in Fig. 14b. It is found that the $I_{T_{BB}}$ time series in the front and rear parts of the envelope of the MJO are multifractal in the said temporal range, as signified by their D_q values. However, the time series along the center axis of the envelope tends to be monofractal since its D_q tends to be constant particularly for $q \geq 1$. At first sight, this D_q spectrum looks qualitatively similar to that obtained by the D_q derived from the 1-point $I_{T_{BB}}$ time series in Fig. 7; however, the causes are totally different. The error bars for this case show that the D_q values are well defined, whereas in Fig. 7, the large error bars suggest uncertainty in D_q estimation due to insufficient sampling.

Figure 14c shows the D_q of time series obtained with the 0.8 threshold. The D_q values in this figure are almost identical to those in Fig. 14b. The dramatic difference between the fractality of the convective intensity in the center of the MJO event and that on its edges is again observed. The fact that the time series on the edges have more significant multifractal features indicates that convective intensity there must be characterized by intermittency. It is known that the cloud clusters embedded in the MJO event often exhibit a burstlike behavior. As shown in Fig. 15, at the map time of 1200 UTC 20 December, maxima of the convective system observed are centered around 160°E. A burst occurs 12 h later, as shown in the following map. Even though the center of maximum convection remains around 160°E with a comparable overall strength, small-scale convective systems are intensified on the peripheral. Such a burst is very likely to be the excitation of smaller-scale waves and disturbances interlocked with the MJO event.

It is interesting to note that even though Fig. 15 or a time–longitude section illustrates that convective intensity varies more on the edges than in the center axis of the MJO, the multifractal analysis in Figs. 13 and 14 further reveals 1) the disturbances and waves embedded in the eastward-moving MJO are interdependent in the range of 1 h to about 5–10 days, characterized by power laws; and 2) the convection on the edges is more intermittent than that in the center and the interdependence of burst events on the edges can be further characterized with power laws.

7. Summary and concluding remarks

In this paper, we examined multiscale tropical deep convective variability in terms of the 4-monthlong hourly high-resolution deep convection index ($I_{T_{BB}}$) obtained during the TOGA COARE IOP over the tropical western Pacific. In the same period, various convection-coupled tropical disturbances, including the diurnal cycle, 2-, 4–5-, and 10-day waves, and the MJO, have been observed in addition to a wide range of background variability (e.g., Tung and Yanai 2002a). Partition functions (M_q) are computed for the $I_{T_{BB}}$ time series [Eq. (4)], at seven different spatial-scale regions from 0.1° × 0.1° to 25° × 25°. It is found that all the partition functions with orders q, mostly concerning $0 \leq q \leq 6$ herein, abide certain power laws in the range of 1 h to ~21.3 days. The power-law exponents, $\tau(q)$, yield a spectrum of generalized dimensions (D_q) for each $I_{T_{BB}}$ time series (Fig. 7). In each case, D_q is a nonlinear, monotonically decaying function of q. Therefore, all seven $I_{T_{BB}}$ time series are multifractal in the range of 1 h to ~21 days.

Although multifractal features exist in all the time series with different degrees of spatial averaging, the larger the spatial averaging, the less nonlinear the D_q function becomes. This indicates that multifractal features can be gradually weakened through area smoothing. Limited by the spatial coverage of the current dataset, the critical domain size for multifractal features

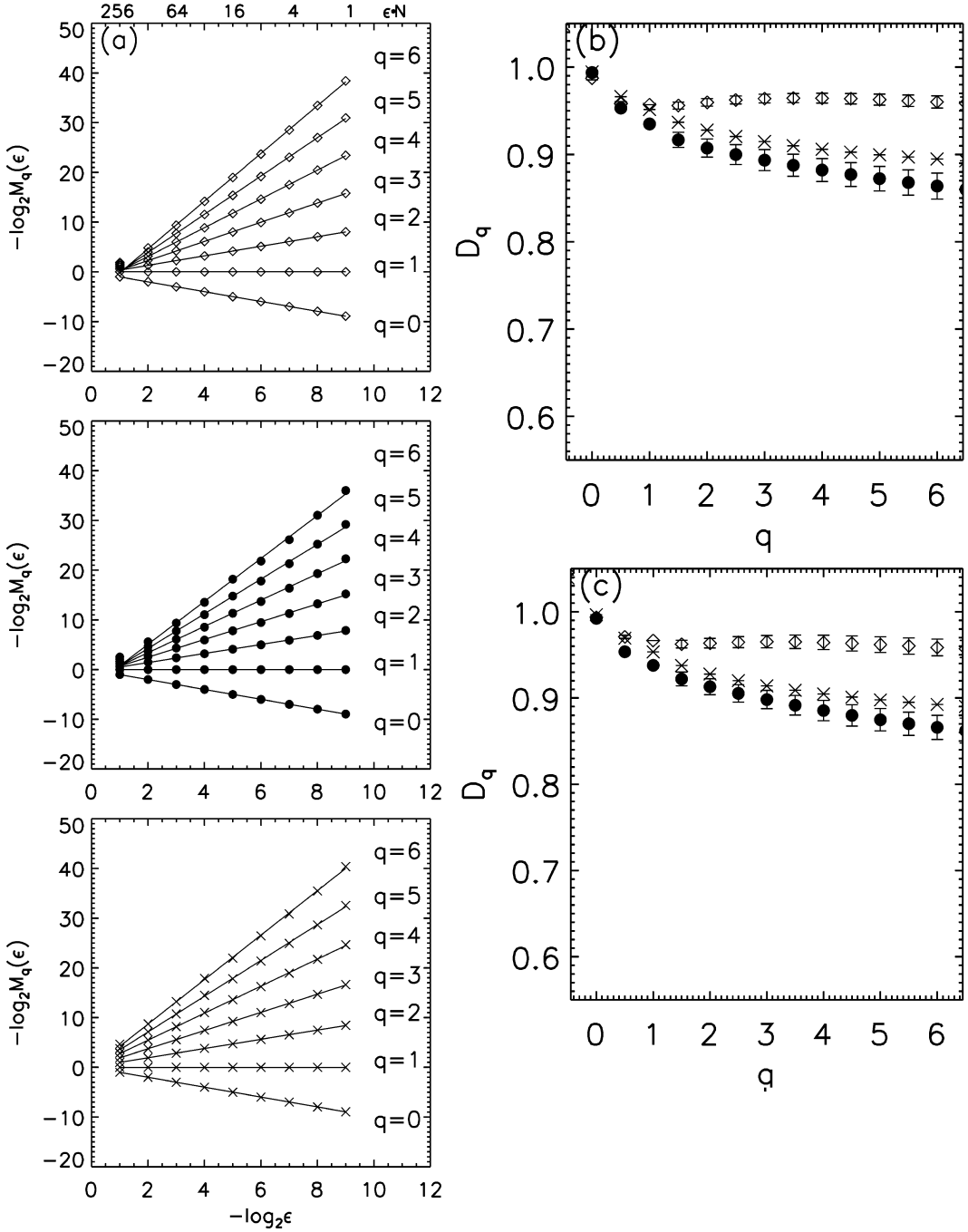

FIG. 14. The partition functions $[M_q(\epsilon)]$ derived from the $I_{T_{BB}}$ in the middle ($\diamond$), front ($\bullet$), and rear ($\times$) parts of the MJO envelope determined by the 0.5 threshold, (a) similar to Fig. 5a. (b), (c) Similar to Fig. 5c but for the generalized dimensions (D_q) of the three time series derived from the 0.5 and 0.8 thresholds, respectively.

to disappear cannot be addressed. Yano et al. (2001) used point-by-point station data during the TOGA COARE IOP and found that convective activities vary as $1/f$ stochastic processes. The results of our spatial-averaging analysis verify their conjecture that the $1/f$ property would remain significant after large-domain averaging.

It is also found that the $I_{T_{BB}}$ time series has the property of long-range dependence, which is characteristic of all multiplicative cascade multifractals (Gao and Rubin 2001). Physically, it is observed that convection associated with smaller-scale waves and disturbances gains intensity during the convective phase of the MJO and undergoes continuous intensification until the end

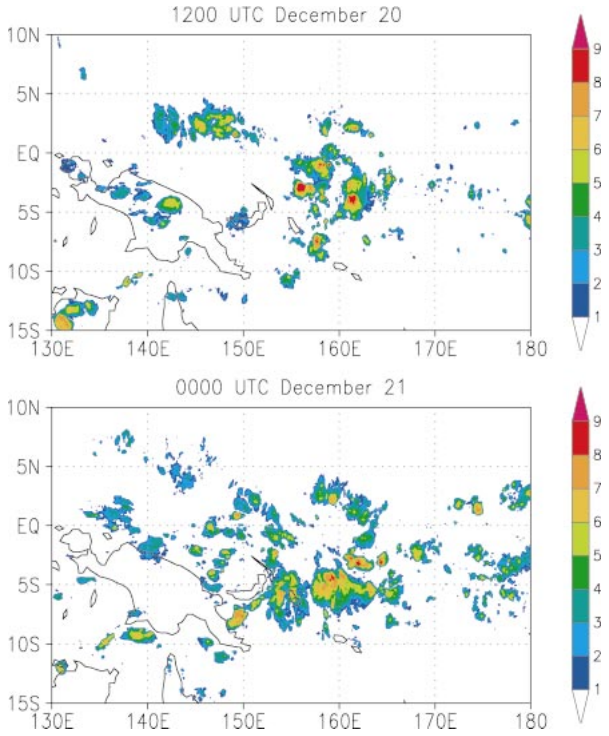

FIG. 15. The $I_{T_{BB}}$ maps (top) at 1200 UTC 20 Dec and (bottom) at 0000 UTC 21 Dec.

of convective phase. When compared with a white noise as well as red noise processes generated by an autoregressive model, the autocorrelation functions (represented by the variance–time plot in Fig. 10) of the $I_{T_{BB}}$ decay with a much slower rate characterized by power laws. This indicates that the physical processes involved have a much longer memory. Hence, when compared with a white or a commonly used red noise with short-range correlations, the transient features in $I_{T_{BB}}$ time series are resilient to temporal smoothing. The result raises concerns over the general practice of using quantities averaged over designated months (e.g., December, January, and February representing the Northern Hemispheric winter) to assess comparisons among model results or between model and observational results. It is important for analysts to realize a priori that the averages in the Tropics may not contain the same certainty as those in the midlatitudes. In the case where the averages in the Tropics are ill defined, alternative comparisons over partition functions and generalized dimensions could provide much meaningful information. Furthermore, it is noted that with larger-spatial averaging, the $I_{T_{BB}}$ time series exhibits an even longer-range dependence, as shown by the variance–time plots as well as the larger D_2 in Fig. 7. This suggests that the effects of larger-scale coherent structures that have longer trends (such as the supercloud clusters associated with the MJO) are more completely captured by the larger-domain averaging.

The evolution of cloud clusters inside the envelope of the first MJO event during the IOP is studied from a Lagrangian standpoint. The center axis of the MJO envelope is determined using two different thresholds of retaining the top 20% and 10% of the deep convective activity. However, the results are not sensitive to the thresholds. Time series along the front, center, and rear of the MJO event show that convection intensifies significantly when approaching the date line. The continuous intensification may be associated with the property of long-range dependence observed in the Eulerian experiments. It is also found that in the range of 1 h to about 5–10 days, the occurrence of tropical disturbances and waves embedded in this MJO are interpendent, characterized by power laws. The convection on the front and rear edges of the MJO event is more intermittent than that in the center. Description of the intermittency, observed as bursting cloud clusters, requires the use of higher-order partition functions and generalized dimensions.

Since convection is a spatiotemporal phenomenon, a more desirable framework to describe convective systems is to characterize their spatiotemporal multifractal properties. The description may start from first characterizing the spatial (temporal) multifractal features of the systems at a fixed time (space), then examining how the features vary with time (space). In more favorable situations, one may obtain some observables, which contain information both on the spatial and temporal complexities of the systems. One can then study the multifractal properties of the systems through those observables. For example, in the study of spatiotemporal chaos through coupled map approaches, a commonly used observable is the mean of the variables on the lattices. That is, one proceeds by calculating dimension densities of this observable (e.g., Bauer et al. 1993; Politi and Witt 1999; Raab and Kurths 2001). However, understanding using this path has been limited. Due to the limited spatial sample size of the data studied here, we have mostly performed temporal multifractal analysis, together with spatial averaging. It is interesting to note that with larger domain spatial averaging, the D_q curves become larger (Fig. 7). Qualitatively this is consistent with the concept of dimension density in the study of spatiotemporal chaos. However, we emphasize that geophysical systems are far more complex than simple spatiotemporal chaotic systems modeled by coupled map lattices. Furthermore, due to the poor spatial sampling of the data, it is impossible to practice the concept of dimension density. At this juncture, we draw readers' attention to the recent work by Pierrehumbert (1996), who used a dataset with 3 times the spatial sample size of ours to examine the spatial multifractal properties of the high cloud variability over the tropical Pacific Ocean.

The multifractal features of the $5° \times 5°$ $I_{T_{BB}}$ time series are closely reproduced quantitatively by the random multiplicative cascade process model, a result with at

least two implications. First, it suggests that mechanisms similar to multiplicative cascade processes might be responsible for the observed multiscale variability. For example, in the atmosphere, convective circulation interacting with its environment could communicate the change of vorticity and momentum from local to larger scales, resulting in continuous stretching and folding of the dynamic and thermodynamic fields. Observational studies have shown evidence of convection modifying large-scale vorticity field through momentum transport (e.g., Shapiro and Stevens 1980; Tollerud and Esbensen 1983; Sui and Yanai 1986; Wu and Yanai 1994; Tung and Yanai 2002b). Other physical processes responsible for the multiscale phenomenon may include but are not limited to nonlinear wave–wave interactions (Hayashi and Golder 1985) and the gravity wave pulses emanating from convective heat source (Mapes 1993). In order to realize the observed tropical convective activities, physical processes, such as the excitation of deep convection and the interaction between convection and waveguides, should also be seriously considered. Second, it should be emphasized that the multiplicative cascade model is nonlocal in time (hence noncausal), which has an immediate consequence that the predictable time scale for the convective systems during the 4-month period the deep convective activities were measured is shorter than the entire period. Physically, this is plausible.

The same kind of multiplicative processes that induce multiscale convective variability in the Tropics may be also present in other convective regions on the earth. However, in the Tropics, the scale-under influence of a process could be maximized by the weak Coriolis force and relatively uniform large-scale thermodynamic variability. As suggested by our study, the multifractal features could be preserved beyond the spatial size of 25° $\times$ 25° and so could the maximum scale of influence. It is reasonable to speculate that such maximum scale is constrained by the latitudinal extent of the warm pool.

The multifractal approach used here has many other applications. It is a potent tool to evaluate model performance, reaching beyond mean and variance to provide information in higher-order statistical moments that are associated with the correlation structure of extreme events. For instance, with longer data records of convective activity, the scaling region (currently from 1 h to about 20 days) could be reexamined and may be extended, particularly to test whether the wide-range variability of MJO in observation can also be described with power laws. The results would be a more quantitative evaluation of current models' ability to produce MJO along with its well-known irregularity and interlocking scales. Finally, a most complex problem in modeling a convecting atmosphere, notably the Tropics, is characterizing interactions among scales. The analysis herein shows that extreme events play an important role in the observed convective variability. From the perspective that cumulus parameterization should represent extreme events and large-scale models such as GCMs are sensitive to the parameterization, subgrid-scale extreme convective events likely have identifiable effects at large scales. The multifractal approach uses few parameters to describe not only the occurrence of the extreme events but also the interdependence of these events: a parsimonious evaluation of cumulus parameterization. The multifractal technique could be used to analyze cloud-system-resolving model datasets of large dynamic range, such as explicit simulations of convectively coupled tropical waves, in order to gain insight into the attendant multiscale interactions.

Acknowledgments. The authors are very grateful to discussions with D. Baker, P. Bechtold, H. Hastings, C. Jeffery, G. Kiladis, J. Lin, C. Liu, H. Liu, M. Montgomery, and R. Plougonven; as well as invaluable suggestions from B. Mapes, J.-I. Yano, and two anonymous reviewers. The high-resolution deep convective index is the courtesy of T. Nakazawa. The leading author also deeply appreciates M. Yanai for stimulating debates while the work began to materialize. This work is supported by the NCAR Advanced Study Program (ASP).

REFERENCES

Bauer, M., H. Heng, and W. Martienssen, 1993: Characterization of spatiotemporal chaos from time-series. *Phys. Rev. Lett.,* **71,** 521–524.

Biferale, L., M. Blank, and U. Frisch, 1994: Chaotic cascades with Kolmogorov 1941 scaling. *J. Stat. Phys.,* **75,** 781–795.

Box, G. E. P., and G. M. Jenkins, 1976: *Time Series Analysis: Forecasting and Control.* 2d ed. Holden-Day, 553 pp.

Chang, C.-P., 1970: Westward propagating cloud patterns in the tropical Pacific as seen from time-composite satellite photographs. *J. Atmos. Sci.,* **27,** 133–138.

Davis, A. B., A. L. Marshak, W. J. Wiscombe, and R. F. Cahalan, 1996: Multifractal characterizations of intermittency in nonstationary geophysical signals and fields—A model-based perspective on ergodicity issues illustrated with cloud data. *Proc. Second Workshop on Nonstationary Random Processes and Their Applications,* San Diego, CA, World Scientific, 97–158.

Frederiksen, R. D., W. J. A. Dahm, and D. R. Dowling, 1997: Experimental assessment of fractal scale similarity in turbulent flows. Part 3. Multifractal scaling. *J. Fluid Mech.,* **338,** 127–155.

Frisch, U., 1995: *Turbulence—The legacy of A. N. Kolmogorov*. Cambridge University Press, 296 pp.

——, and G. Parisi, 1985: Fully developed turbulence and intermittency. *Turbulence and Predictability in Geophysical Fluid Dynamics and Climate Dynamics (International School of Physics Énrico Fermi, Course 88),* M. Ghil, R. Benzi, and G. Parisi, Eds., North-Holland, 71–88.

Gao, J. B., and I. Rubin, 2001: Multiplicative multifractal modelling of long-range-dependent network traffic. *Int. J. Comm. Syst.,* **14,** 783–801.

Gouyet, J.-F., 1996: *Physics and Fractal Structures.* Springer-Verlag, 234 pp.

Halsey, T. C., M. H. Jensen, L. P. Kadanoff, I. Procaccia, and B. Shraiman, 1986: Fractal measures and their singularities: The characterization of strange sets. *Phys. Rev. A,* **33,** 1141–1151.

Hayashi, V., and D. G. Golder, 1985: Nonlinear energy transfer between stationary and transient waves simulated by a GFDL spectral general circulation model. *J. Atmos. Sci.,* **42,** 1340–1345.

Hentschel, H. G. E., and I. Procaccia, 1983: The infinite number of

generalized dimensions of fractals and strange attractors. *Physica D,* **8,** 435–444.
Ivanova, K., and T. Ackerman, 1999: Multifractal characterization of liquid water in clouds. *Phys. Rev.,* **59E,** 2778–2782.
Kaulakys, B., and T. Meskauskas, 1998: Modeling 1/f noise. *Phys. Rev. E,* **58,** 7013–7019.
Kolmogorov, A. N., 1941: The local structure of turbulence in incompressible viscous fluid for very large Reynolds number. *Dokl. Akad. Nauk SSSR,* **30,** 299–303.
Lau, K.-M., T. Nakazawa, and C. H. Sui, 1991: Observations of cloud cluster hierarchies over the tropical western Pacific. *J. Geophys. Res.,* **96,** 3197–3208.
Lilly, D. K., 1983: Stratified turbulence and the mesoscale variability of the atmosphere. *J. Atmos. Sci.,* **40,** 749–761.
Lin, J. W.-B., and J. D. Neelin, 2002: Considerations for stochastic convective parameterization. *J. Atmos. Sci.,* **59,** 2793–2823.
Madden, R. A., and P. R. Julian, 1971: Detection of a 40–50-day oscillation in the zonal wind in the tropical Pacific. *J. Atmos. Sci.,* **28,** 702–708.
Mallat, S. G., 1999: *A Wavelet Tour of Signal Processing.* 2d ed. Academic Press, 637 pp.
Mandelbrot, B. B., 1974: Intermittent turbulence in self-similar cascades: Divergence of high moments and dimension of the carrier. *J. Fluid Mech.,* **62,** 331–358.
——, 1982: *The Fractal Geometry of Nature.* Freeman, 468 pp.
——, and J. W. Van Ness, 1968: Fractional Brownian motions, fractional noises and applications. *SIAM Rev.,* **10,** 422–437.
Mapes, B. E., 1993: Gregarious tropical convection. *J. Atmos. Sci.,* **50,** 2026–2037.
Marsan, D., D. Schertzer, and S. Lovejoy, 1996: Causal space–time multifractal processes: Predictability and forcasting of rain fields. *J. Geophys. Res.,* **101,** 26 333–26 346.
Matsuno, T., 1966: Quasi-geostrophic motions in the equatorial area. *J. Meteor. Soc. Japan,* **44,** 25–43.
Monin, A. S., and A. M. Yaglom, 1975: *Statistical Fluid Mechanics.* Vol. 2. MIT Press, 874 pp.
Murakami, M., 1983: Analysis of the deep convective activity over the Western Pacific and Southeast Asia. Part I: Diurnal variation. *J. Meteor. Soc. Japan,* **61,** 60–76.
Nakazawa, T., 1988: Tropical super clusters within intraseasonal variations over the western Pacific. *J. Meteor. Soc. Japan,* **66,** 823–839.
——, 1995: Intraseasonal oscillations during the TOGA-COARE IOP. *J. Meteor. Soc. Japan,* **73,** 305–319.
Over, T. M., and V. K. Gupta, 1996: A space–time theory of mesoscale rainfall using random cascades. *J. Geophys. Res.,* **101,** 26 319–26 331.
Perica, S., and E. Foufoula-Georgiou, 1996: Model for multiscale disaggregation of spatial rainfall based on coupling meteorological and scaling descriptions. *J. Geophys. Res.,* **101,** 26 347–26 361.
Pierrehumbert, R., 1996: Anomalous scaling of high cloud variability in the tropical Pacific. *Geophys. Res. Lett.,* **23,** 1095–1098.
Politi, A., and A. Witt, 1999: Fractal dimension of space–time chaos. *Phys. Rev. Lett.,* **82,** 3034–3037.
Raab, C., and J. Kurths, 2001: Estimation of large-scale dimension densities. *Phys. Rev. E,* **64,** 016216.
Salby, M. L., and H. H. Hendon, 1994: Intraseasonal behavior of clouds, temperature, and motion in the Tropics. *J. Atmos. Sci.,* **51,** 2207–2224.
Schmitt, F., S. Vannitsem, and A. Barbosa, 1998: Modeling of rainfall time series using two-state renewal processes and multifractals. *J. Geophys. Res.,* **103,** 23 181–23 193.
Shapiro, L. J., and D. E. Stevens, 1980: Parameterization of convective effects on the momentum and vorticity budgets of synoptic-scale Atlantic tropical waves. *Mon. Wea. Rev.,* **108,** 1816–1826.
Sui, C. H., and M. Yanai, 1986: Cumulus ensemble effects on the large-scale vorticity and momentum fields of GATE. Part I: Observational evidence. *J. Atmos. Sci.,* **43,** 1618–1642.
Takayabu, Y. N., 1994: Large-scale cloud disturbances associated with equatorial waves. Part I: Spectral features of the cloud disturbances. *J. Meteor. Soc. Japan,* **72,** 433–449.
——, and T. Nitta, 1993: 3–5 day period disturbances coupled with convection over the tropical Pacific Ocean. *J. Meteor. Soc. Japan,* **71,** 221–246.
Tollerud, E. I., and S. K. Esbensen, 1983: An observational study of the upper-tropospheric vorticity fields in GATE cloud clusters. *Mon. Wea. Rev.,* **111,** 2161–2175.
Tung, W.-W., and M. Yanai, 2002a: Convective momentum transport observed during the TOGA COARE IOP. Part I: General features. *J. Atmos. Sci.,* **59,** 1857–1871.
——, and ——, 2002b: Convective momentum transport observed during the TOGA COARE IOP. Part II: Case studies. *J. Atmos. Sci.,* **59,** 2535–2549.
Veneziano, D., R. L. Bras, and J. D. Niemann, 1996: Nonlinearity and self-similarity of rainfall in time and a stochastic model. *J. Geophys. Res.,* **101,** 26 371–26 392.
Webster, P. J., and R. Lukas, 1992: TOGA COARE: The coupled ocean–atmosphere response experiment. *Bull. Amer. Meteor. Soc.,* **73,** 1377–1416.
Weng, H., and K.-M. Lau, 1994: Wavelets, period doubling, and time-frequency localization with application to organization of convection over the tropical western Pacific. *J. Atmos. Sci.,* **51,** 2523–2541.
Wheeler, M., and G. N. Kiladis, 1999: Convectively coupled equatorial waves: Analysis of clouds and temperature in the wavenumber-frequency domain. *J. Atmos. Sci.,* **56,** 374–399.
Wu, X., and M. Yanai, 1994: Effects of vertical wind shear on the cumulus transport of momentum: Observations and parameterization. *J. Atmos. Sci.,* **51,** 1640–1660.
Yanai, M., B. Chen, and W.-W. Tung, 2000: The Madden–Julian oscillation observed during the TOGA COARE IOP: Global view. *J. Atmos. Sci.,* **57,** 2374–2396.
Yano, J.-I., and Y. Takeuchi, 1987: The self-similarity of horizontal cloud pattern in the intertropical convergence zone. *J. Meteor. Soc. Japan,* **65,** 661–667.
——, and N. Nishi, 1989: The hierarchy and self-affinity of the time variability within the tropical atmosphere inferred from the NOAA OLR data. *J. Meteor. Soc. Japan,* **67,** 771–789.
——, J. C. McWilliams, and M. W. Moncrieff, 1996: Fractality in idealized simulations of large-scale tropical cloud systems. *Mon. Wea. Rev.,* **124,** 838–848.
——, K. Fraedrich, and R. Blender, 2001: Tropical convective variability as 1/f noise. *J. Climate,* **14,** 3608–3616.